We are IntechOpen,
the world's leading publisher of
Open Access books
Built by scientists, for scientists

6,900
Open access books available

185,000
International authors and editors

200M
Downloads

154
Countries delivered to

Our authors are among the

TOP 1%
most cited scientists

12.2%
Contributors from top 500 universities

CLARIVATE ANALYTICS
BOOK CITATION INDEX
INDEXED

WEB OF SCIENCE™

Selection of our books indexed in the Book Citation Index
in Web of Science™ Core Collection (BKCI)

Interested in publishing with us?
Contact book.department@intechopen.com

Hyperspectral Imaging:
a New Modality in Surgery

Hamed Akbari and Yukio Kosugi
Tokyo Institute of Technology
Japan

1. Introduction

Nowadays medical diagnosis is principally supported by the imaging techniques. Several imaging modalities such as magnetic resonance imaging (MRI), computed tomography (CT), ultrasonography, Doppler scanning, and nuclear imaging have completely expanded medical imaging field. Recently Hyperspectral imaging (HSI), has emerged as a new member of the family of the medical imaging modalities. HSI provides a powerful tool for non-invasive tissue analyses. This technology is able to capture both the spatial and spectral data of an organ or tissue in one snapshot. In other words, the imaging system produces many narrow band images at different wavelengths. Not similar to conventional three-channel color cameras and other filter-based imaging systems, this system captures full neighboring spectral data with spectral and spatial information (Akbari et al., 2008a).

HSI can visualize invisible wavelength regions and bring them to the human vision range. Pervious decades, hyperspectral imaging was a complicated technique that was employed in satellite or aircraft systems. However, this technology has been customized to a compact imaging and spectroscopy tool with potential applications in medicine. In fact, Hyperspectral imaging has already been applied in the medical field. Kellicut et al. utilized HSI to quantitatively evaluate the tissue oxygen saturation in patients with peripheral vascular disease (Kellicut et al., 2004). Khaodhiar et al. employed this imaging technique to predict and follow healing in foot ulcers of diabetic patients (Khaodhiar et al., 2007). HSI was used to diagnose hemorrhagic shock (Cancio et al., 2006), to detect chronic mesenteric ischemia during endoscopy (Friedland et al., 2007), and to detect skin cancer in mice (Martin et al., 2006).

Hyperspectral imaging captures reliable data for the surgeons in the operating room with a convenient instrument. It shows a greater sensitivity for detecting a residual tumor tissue than current surgical tissue sampling techniques (Freeman et al., 2005). Monteiro et al. employed this technique to enhance the regions covered with a layer of blood during surgeries (Monteiro et al., 2006). HSI is utilized to detect ischemic regions of the intestine during surgery (Akbari et al., 2008b). A hyperspectral imaging endoscope is used for the early detection of dysplasia and cancer in lung epithelia (Lindsley et al., 2004). Zuzak et al. coupled a surgical laparoscope for conventional minimally invasive surgical procedures with a near-infrared hyperspectral imaging system to help guide laparoscopic surgeons to visualize biliary anatomy (Zuzak et al., 2007).
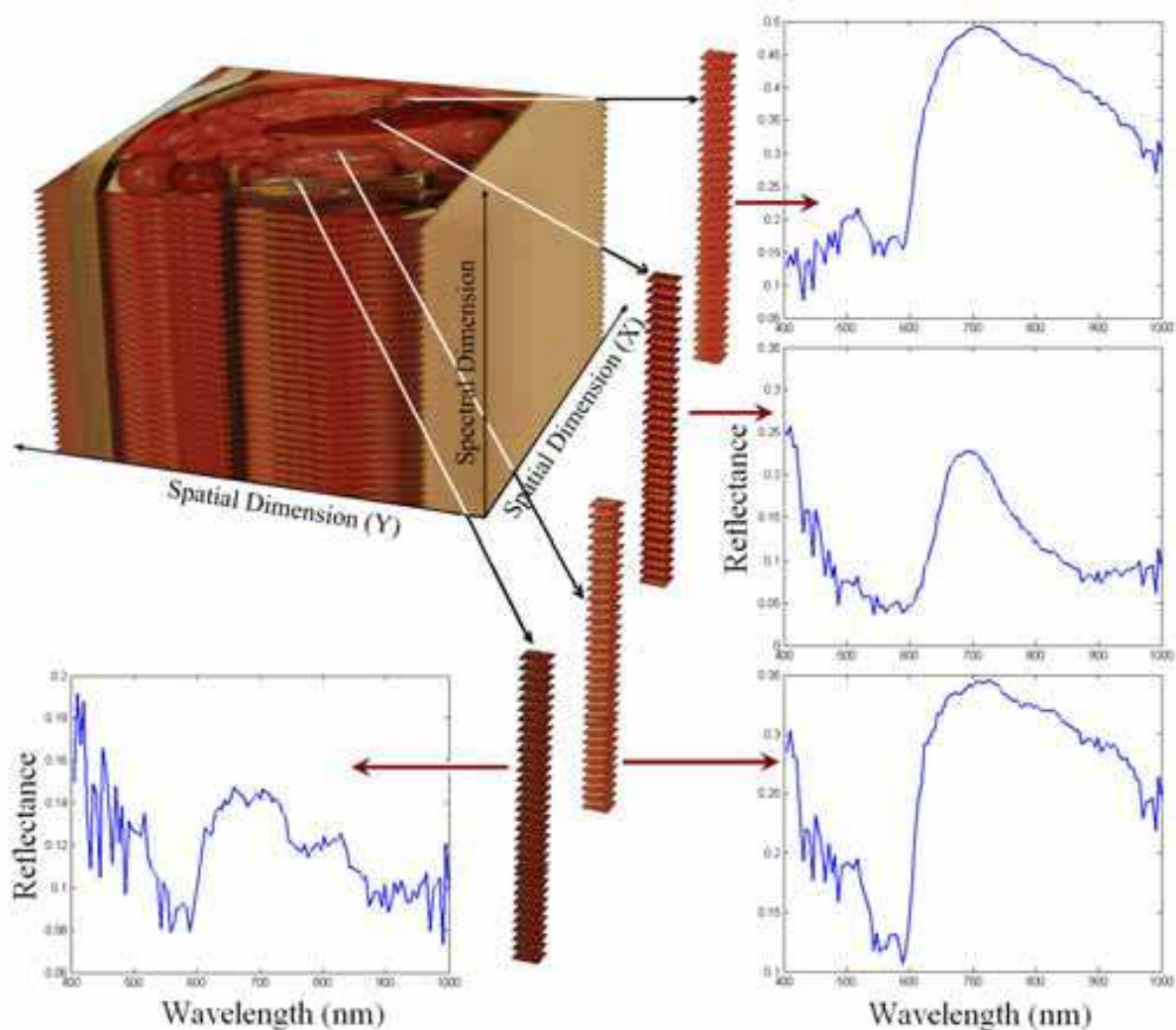
Fig. 1. A schematic view of a hyperspectral image of pig's abdomen is shown. The spectral graph of the average spectrum from the pig's peritoneum, spleen, colon, and urinary bladder are shown in the four graphs. The graph depicts the reflectance for each wavelength in that region.

This chapter presents the application of hyperspectral imaging as a visual supporting tool to detect different organs and tissues during surgeries. Diagnosis of abnormal tissue or tissues which are not in natural anatomic location is an important concern in surgeries. Hyperspectral imaging can be a useful technology for finding ectopic tissues and diagnosis of tissue abnormalities such as intestinal ischemia. The ectopic or heterotopic tissue, particularly when missed, can cause complications in patients. Intestinal ischemia results from a variety of disorders that cause insufficient blood flow to the intestine. The type and prognosis of ischemic injury depend on the blood vessels involved, the underlying medical condition, and the swiftness with which the problem is brought to medical attention for diagnosis and treatment.

2. Hyperspectral Imaging

Hyperspectral imaging captures and analyses data from across the electromagnetic spectrum. This technology extends the human vision that just sees visible light. Hyperspectral imaging can visualize the visible light as well as near-infrared to infrared.

The difference between hyperspectral and multi-spectral imaging is usually defined according to the number of spectral bands. Multi-spectral image contains tens of bands. However, hyperspectral image contains hundreds to thousands of bands. Hyperspectral images are captured by one sensor that captures a set of contiguous bands. However, multi-spectral is a set of spectral bands that are not typically contiguous and can be captured by multiple sensors. Figure 1 shows a schematic view of the hyperspectral image.
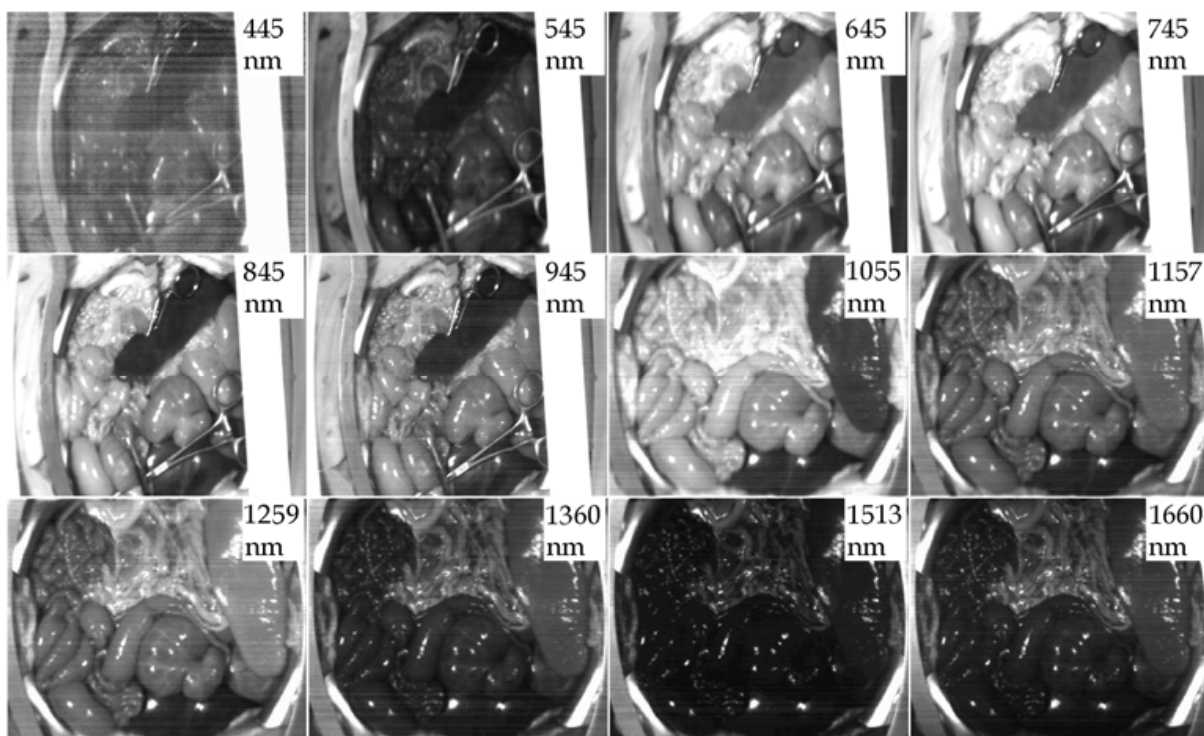

Fig. 2. Several images at different wavelengths during an abdominal surgery on pigs.

Two hyperspectral sensors were used to capture the image data for segmentation of abdominal organs and detection of intestinal ischemic tissue: an ImSpector N17E and a V10E, manufactured by Spectral Imaging Ltd., Oulu, Finland. The hyperspectral systems have more than hundred bands and high spectral resolution. Hyperspectral sensors generate a two-dimensional spatial image along a third spectral dimension. Each pixel in the hyperspectral image has a sequence of reflectance in different spectral wavelengths that can display the spectral signature of that pixel. Since there are a large number of data for each image, artificial neural networks and machine classifiers along with wavelet compression were used to segment the images. The technique was evaluated during the abdominal surgeries on two pigs under general anesthesia. In this research, using the hyperspectral cameras, the spectral signatures for abdominal organs has been created. Using these signatures, the abdominal view through a large incision is segmented. Figure 2 shows the

images in different wavelengths that are captured using two cameras in a large-incision view during the abdominal surgery on the pigs.

2.1 Hyperspectral sensors

The hyperspectral sensors are instruments for capturing many images in different adjacent wavelengths of an illuminated region corresponding to the entrance slit. The main components of a hyperspectral camera are shown in Figure 3. As light sources, two halogen lamps illuminate the object to be captured. The camera's objective lens collects the radiation from the object and projects an image on the entrance slit plane. The slit determines the instantaneous field of imaging in spatial directions. The radiation from the slit is projected to the prism-grating-prism (PGP) components (ImSpector optics). Therefore, the propagation angle of the radiation changes depending on its wavelength. Then it is focused on the matrix detector. Every object's point is represented on the matrix detector by a series of monochromatic points that makes a continuous spectrum in the direction of the spectral axis. For example, an instantaneous image of the AB line is captured as the lines A1B1, A2B2,…, AnBn, where "n" is the wavelength band number.
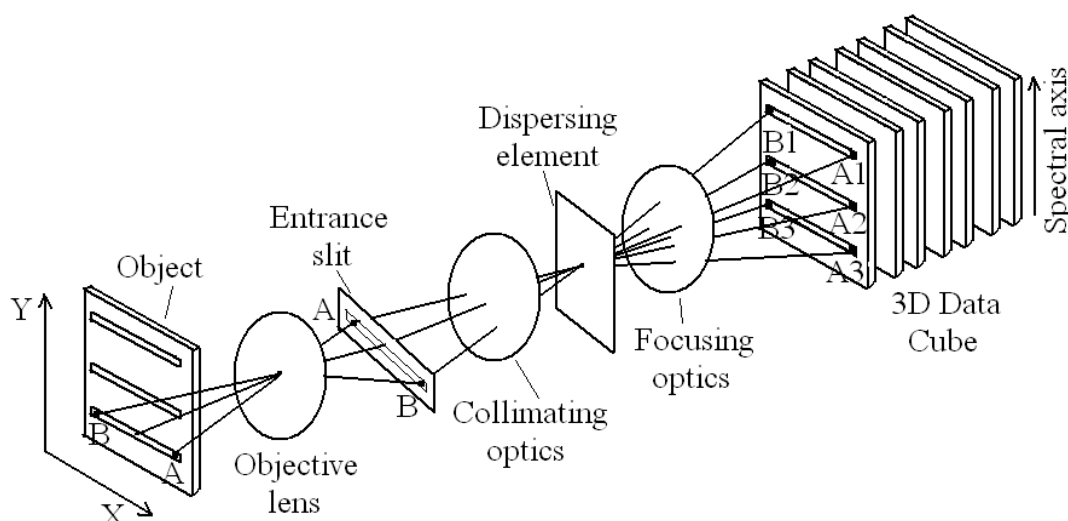

Fig. 3. Design of the hyperspectral imaging sensor (Aikio, 2001)

Whisk-broom scanning, filtered imaging, and push-broom are three main designs for hyperspectral cameras. Whisk-broom scanner captures the spectral dimension pixel-to-pixel. Filtered camera captures two spatial dimensions and temporally samples the spectral dimension. The capturing technique of ImSpector sensors is a push-broom scanning. In this type of imaging spectrometer, the entrance slit limits the imaging field. The 2D detector matrix instantaneously captures the spectral dimension and one spatial dimension. The second spatial dimension is generated by scanning the object. By moving the camera's field of view relative to the object, the second spatial dimension is created. Figure 4 shows a schematic of the imaging techniques.
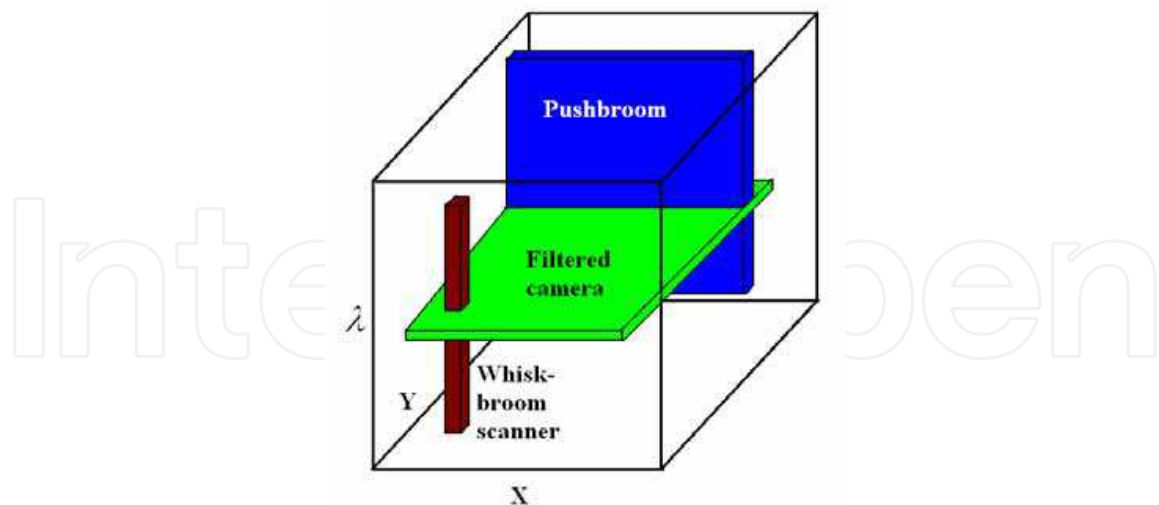
Fig. 4. A schematic of the hyperspectral image capturing techniques (Aikio, 2001)

The PGP is composed of a special grating, two prisms, and an aperture stop. The special grating is located between two prisms and the aperture stop is set in contact with the grating. Short and long pass filters are usually placed between the grating and the prisms, eliminating unwanted wavebands and changing the spectral response. In this technique, since the filters are incorporated inside a PGP, the reflections from their surfaces can be eliminated. Unlike a direct vision prism where the dispersion is a non-linear small dispersion, the diffraction grating in the PGP supplies a large linear dispersion (Aikio, 2001). Using two cameras, the ImSpector N17E and the V10E, the wavelength range of 400 - 1700 nm may be captured. The V10E model captures the spectral range of 400 - 1000 nm, a dispersion of 97.5 nm/mm, and a spectral resolution of 5 nm (with a 30 µm slit). The N17E sensor captures the spectral range of 900 - 1700 nm, a dispersion of 110nm/mm, and a spectral resolution of 5 nm (with a 30 µm slit). All the wavelengths will be passed for only the small region of the object that is exactly in front of the entrance slit. By shifting the sensor between subsequent images, ultimately all parts of the object and all corresponding wavelengths are captured. Therefore, for each wavelength, a monochromatic spectral image can be constructed from the hyperspectral image set.

2.2 Capturing setup
The ImSpector sensors capture the images using the push-broom scanning technique. Therefore, to generate the second spatial dimension the object must be scanned i.e. the second spatial dimension is captured by moving the camera's field of view relative to the object. The linear actuator, a ROBO Cylinder Slider (model RCS-SM-A-100-H-1000-T1-S), is used to move the camera. This actuator is controlled by an XSEL-J-1-100A-N3-EEE-2-1 type controller. The actuator and controller are manufactured by IAI Corporation, Japan. The actuator works with a ball screw drive system, a 100 W motor, and an absolute incremental encoder. The actuator has an 84.9 N rated thrust, a 1-1000 mm/s speed, a ±0.02 mm positioning repeatability, and a maximum backlash of 0.05 mm. The actuator is connected to the controller by two cables: the encoder cable and the motor cable. The movement and velocity are adjusted by a setting tool that is connected to the controller. The actuator moves the camera with a constant velocity.

Fig. 5. The acquisition setup

The acquisition setup consists of a pair of 500 W halogen lamps with diffusing reflectors as the light sources and the computer-controlled linear actuator. The linear actuator is fixed on a bridge installed over the surgical bed and the camera has been calibrated and fixed on the frame. Therefore, the distance between the lens and the abdomen is constant and a fairly uniform illumination of the subject is provided by using the two halogen lamps. Figure 5 shows the acquisition setup.

2.3 Data normalization

The captured data should be normalized to treat the spectral non-uniformity of the illumination device. The raw data are changed by illumination conditions and temperature. Therefore, the radiance data were normalized to yield the radiance of the specimen.

White reference and dark current are two data that should be captured for normalization. White reference is the spectrum acquired by the hyperspectral sensor corresponding to the white reference and dark current is a dark image acquired by the system in the absence of light. Figure 6 shows a spectral signature and corresponding white reference and dark current. White reference is used to show the maximum reflectance in each wavelength. Dark current spectroscopy is used to address the defects by calculating the peaks in the dark current spectrum with temperature. To perform this pre-processing step, the radiance of a standard reference white board placed in the scene and the dark current are measured by keeping the camera shutter closed.
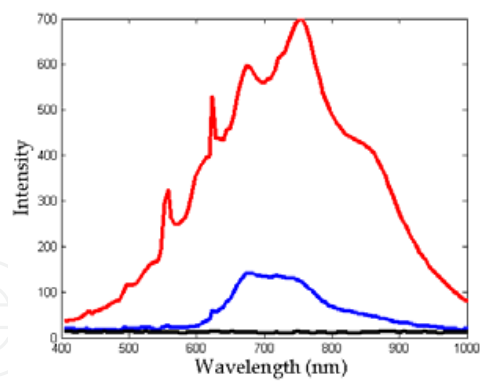
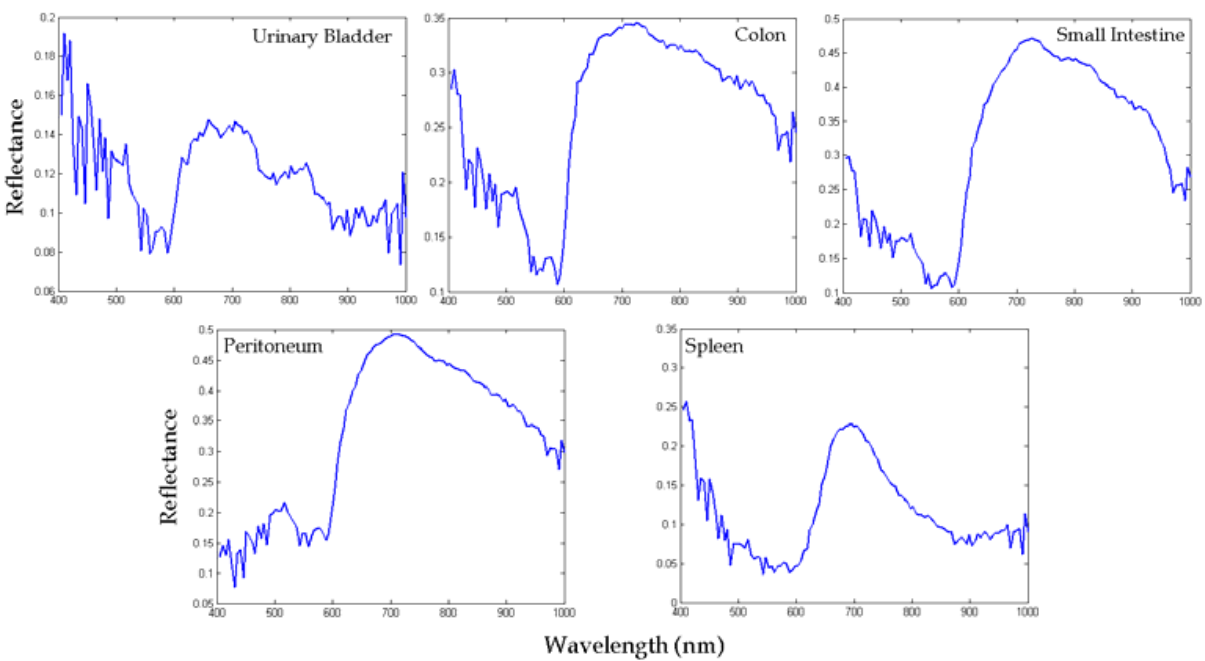Fig. 6. A spectral signature in blue and corresponding white reference in red and dark current in black.

Fig. 7. Reflectance spectra using visible and near infrared camera: the horizontal axis shows different wavelengths in nanometers, and the vertical axis shows the reflectance.

Then the raw data are corrected to reflectance using the following equation:

$$R(\lambda) = \frac{I_{raw}(\lambda) - I_{dark}(\lambda)}{I_{white}(\lambda) - I_{dark}(\lambda)} \qquad (1)$$

where $R(\lambda)$ is the calculated reflectance value for each wavelength, $I_{raw}(\lambda)$ is the raw data radiance value of a given pixel, and $I_{dark}(\lambda)$ and $I_{white}(\lambda)$ are, respectively, the dark current and the white board radiance acquired for each line and spectral band of the sensor. The dark current and white reference in the ImSpector N17E sensor is separately captured and included in the main *.raw data file. However, in the ImSpector V10E, it was captured in a separate file in *.drk format. The white reference board should be placed in the

capturing field when the ImSpector V10E is used. However, the dark current should be captured separately. Figure 7 and Figure 8 show the reflectance spectra of the abdominal organs.
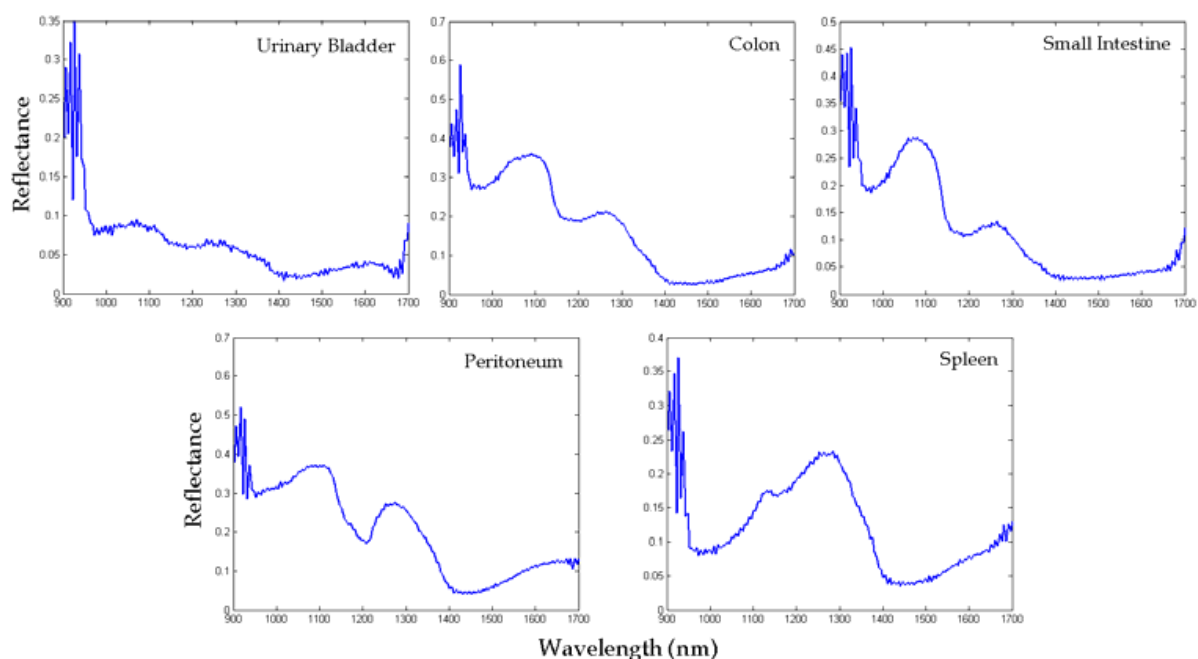

Fig. 8. Reflectance spectra using near infrared and infrared camera: the horizontal axis shows different wavelengths in nanometers, and the vertical axis shows the reflectance.

3. Segmentation of Abdominal Organs

Due to the ambiguity between the organ and its adjacent tissues, it is difficult to segment the organs and tissues during surgeries. Due to the movements of the object, dynamic situations such as in live and/or moving subjects will worsen the detection (Liu et al., 2007). In special situations such as anatomic variations, ectopic tissues, and tissue abnormalities, this problem becomes more challenging. Hyperspectral imaging is used to segment the abdominal organs during the surgeries on two pigs. Two approaches are utilized to classify the hyperspectral data. In the first approach, the data are compressed via wavelet decomposition then classified using learning vector quantization (LVQ) (Akbari et al., 2008a). In the second approach, the data are classified by a support vector machine (SVM) (Akbari et al., 2009).

3.1 Normalized difference indexes

Hyperspectral images may be visualized in a real-time manner using the normalized difference index (NDI). This is a simple method to enhance organs or tissues in hyperspectral data. NDI has been employed in many research studies to estimate chlorophyll content (Richardson et al. 2002), to evaluate the effects of nitrogen fertilization treatments (Moran et al. 2000), to estimate water content (Datt et al., 2003), and to estimate the yields of salt- and water-stressed forages (Poss et al., 2006).
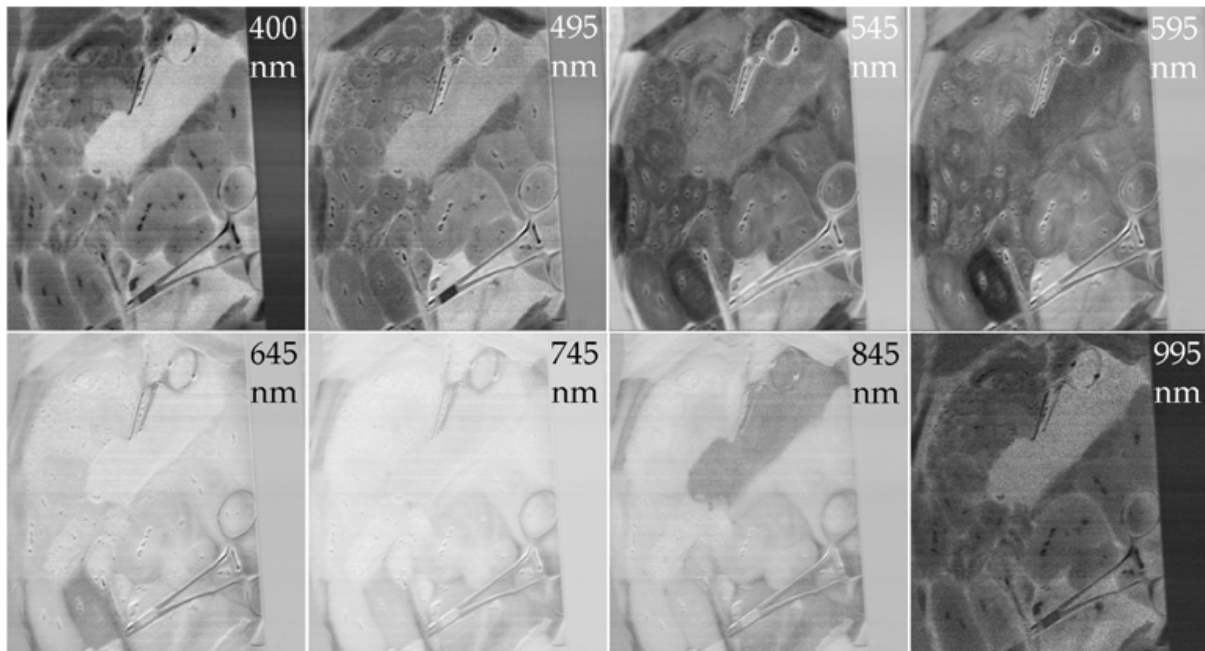
Fig. 9. Eight sample images using the proposed NDI at different wavelengths using visible and near infrared camera (400-1000 nm).

Many combinations of the reflectance and intensity were evaluated to find the appropriate NDI. Each NDI can enhance one or several organs. Several combinations of wavelengths were selected to enhance the difference of organs or tissues. The following equation is applied to calculate the NDI in the hyperspectral data in 400-1000 nm:

$$\text{NDI}(\lambda) = \frac{\text{I}(\lambda) - \text{I}(945\text{nm})}{\text{I}(\lambda) + \text{I}(945\text{nm})} \tag{2}$$

where NDI(λ) is the normalized difference index in the wavelength λ and I(λ) is the intensity of a given pixel in the wavelength λ. Figure 9 shows this normalized difference index images in some sample wavelengths. The equation that is utilized to calculate the NDI in 900-1700 nm hyperspectral data is as follows:

$$\text{NDI}(\lambda) = \frac{\text{R}(\lambda) - \text{R}(1660\text{nm})}{\text{R}(\lambda) + \text{R}(1660\text{nm})} \tag{3}$$

where NDI(λ) is the normalized difference index in the wavelength λ and R(λ) is the intensity of a given pixel in the wavelength λ. Figure 10 shows this normalized difference index images in some sample wavelengths. Although this technique is a fast method for visualization, it does not result in precise segmentation in the image processing. Therefore, for the image segmentation, the hyperspectral data were processed by the image processing techniques.
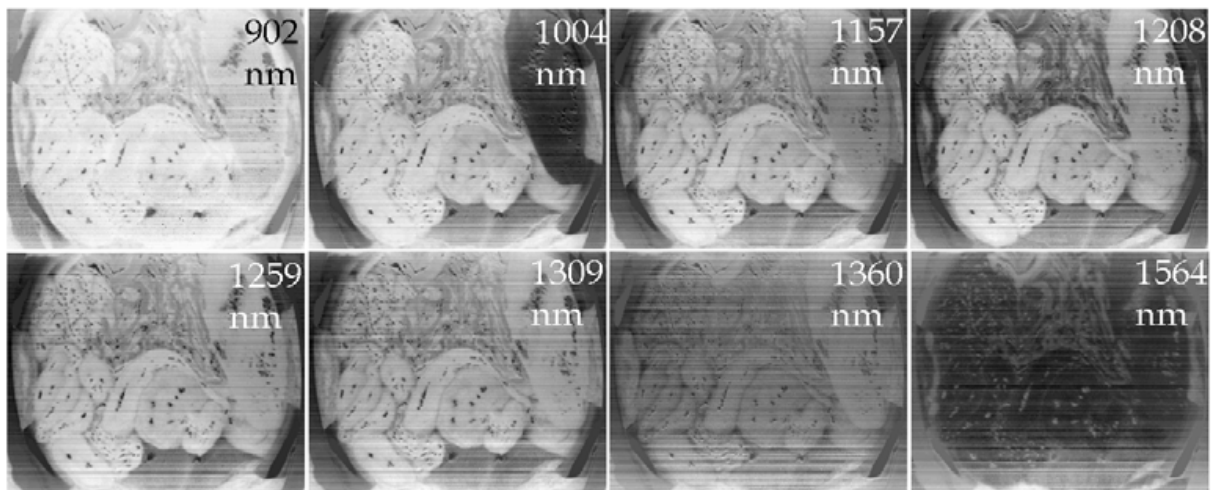
Fig. 10. Eight sample images using the proposed NDI at different wavelengths using near infrared and infrared camera

3.2 Wavelet compression and LVQ classification

Since there is a large quantity of data for each image, it is better to compress the data before processing. In this study, a wavelet transform is used for data compression and LVQ is used to segment the image. Wavelet transform may be used as a type of signal compression for compressing the spectral data. The elements of a signal can be represented by a smaller amount of data. The wavelet transform produces as many coefficients as there are data in the signal, then these coefficients can be compressed. The information is statistically concentrated in just a few coefficients. The wavelet compression is based on the concept that the regular signal component can be accurately approximated using a small number of approximation coefficients and some of the detail coefficients (Chui, 1993; Daubechies, 1992).
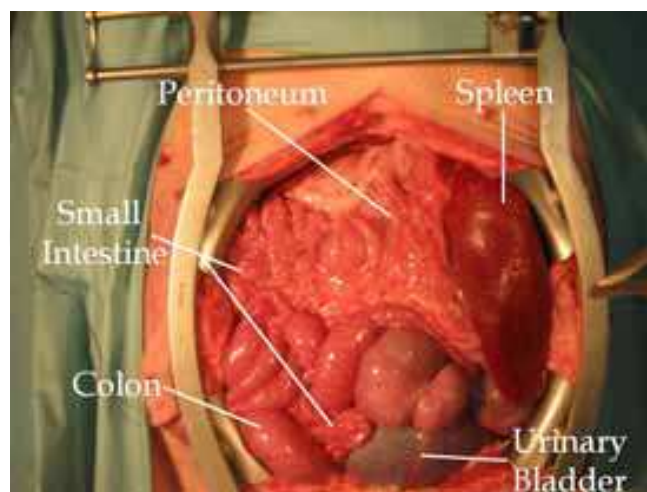

Fig. 11. A large-incision view during an abdominal surgery on pigs

Self-organizing networks can learn to detect regularities and correlations in their input and adapt their future responses to that input accordingly. The neurons of competitive networks

learn to recognize groups of similar input vectors. LVQ is a method for training competitive layers in a supervised manner (Kohonen, 1987). The wavelet-based compressed spectral signatures are the input vectors. The abdominal organs are assigned to be the output of the neural network. The input vectors are correlated to one of seven classes corresponding to the spleen, peritoneum, urinary bladder, small intestine, colon, background, and ambiguous regions. After classification, the pixels which were detected as ambiguous pixels were labeled in the post-processing steps. Figure 11 shows a large-incision view during an abdominal surgery on a pig.

3.3 Support vector machines (SVMs)

Hyperspectral image classification using SVMs has shown superior performance to the other available classification methods (Camps-Valls & Bruzzone, 2005) (Camps-Valls et al., 2004) (Melgani & Bruzzone, 2004) (Huang et al., 2002) (Brown et al., 2000). Multilayer perceptron (MLP) and radial basis function neural networks (RBFNNs) are successful approaches to classify hyperspectral data. However, the high number of spectral bands results in the Hughes phenomenon (Hughes, 1968). Support vector machines (SVMs) can efficiently handle large input spaces or noisy samples (Camps-Valls & Bruzzone, 2005). SVMs use a small number of exemplars selected from the tutorial dataset to enhance the generalization ability. The SVMs are supervised classifiers that have a pair of margin zones on both sides of the discriminate function. The SVM is a popular classifier based on statistical learning theory as proposed by Vapnik (Vapnik, 1995; Brown et al., 2000). The training phase tries to maximize the margin of hyperplane classifier with respect to the training data.

Since the spectral data are not linearly separable, the kernel method is used. Kernel-based methods map data from an original input feature space to a kernel feature space of a higher dimensionality and then solve a linear problem in that space. The Least Squares SVM (LS-SVM), a new version of the SVM, is used for classification (Bao & Liu, 2006; Camps-Valls & Bruzzone, 2005; Liu et al., 2007). A convex quadratic program (QP) solves the classification problem in the SVMs. In LS-SVMs, instead of inequality constraints, a two-norm with equality is applied (Suykens & Vandewalle, 1999). Therefore, instead of a QP problem in dual space, a set of linear equations is obtained. The SVM tries to find a large margin for classification. However, the LS-SVM looks for a ridge regression for classification with binary targets. The selection of hyperparameters is not as problematic and the size of the matrix involved in the QP problem is also directly proportional to the number of training points (Van Gestel et al., 2004). The optimization function of the SVM is modified as follows:

$$\underset{w,b,e}{\text{Min}} \ f(w,e) = \frac{1}{2} w^T w + \gamma \frac{1}{2} \sum_{i=1}^{N} e_i^2 \qquad (4)$$

subject to the equality constraints

$$y_i [w^T \varphi(x_i) + b] = 1 - e_i, \qquad i = 1,...,N \qquad (5)$$

where w is the weighting vector, b is the bias term, e is for misclassifications, and γ is the tuning parameter. This constrained optimization problem can be solved by determining the saddle points in the Lagrange functional as:

$$L(w,b,e;\alpha) = f(w,b,e) - \sum_{i=1}^{N} \alpha_i \{y_i[w^T \varphi(x_i) + b] - 1 + e_i\} \qquad (6)$$

where $\alpha_i \in R$ are Lagrange multipliers that can be positive or negative in the LS-SVM formulation. It is possible to choose many types of kernel functions including linear, polynomial, radial basis function (RBF), multilayer perceptron (MLP) with one hidden layer, and splines. The RBF kernel used in this study was as follows:

$$K(x,x_i) = \exp\{-\|x - x_i\|_2^2 / \sigma^2\} \qquad (7)$$

where σ is constant.

Multi-class categorization problems are represented by a set of binary classifiers. To prepare a set of input/target pairs for training, 100 pixels of data from each region in the surgical hyperspectral images are captured. The SVMs are applied one by one to the image for each class, and each pixel was labeled as an organ (Akbari et al., 2009).

3.4 Experimental results

The experiment was done on two pigs under general anesthesia. A large incision was created on the abdomen, and the internal organs were explored. Vital signs were evaluated during the surgery to assure constant oxygen delivery to the organs. Nine hyperspectral images by the ImSpector N17E and seven hyperspectral images by the ImSpector V10E were captured. The actuator velocity was set such that the resolutions of the two spatial dimensions were equal. The performance (i.e. the quality of detection) was evaluated with respect to the hand-created maps produced by a medical doctor and by using anatomical data.
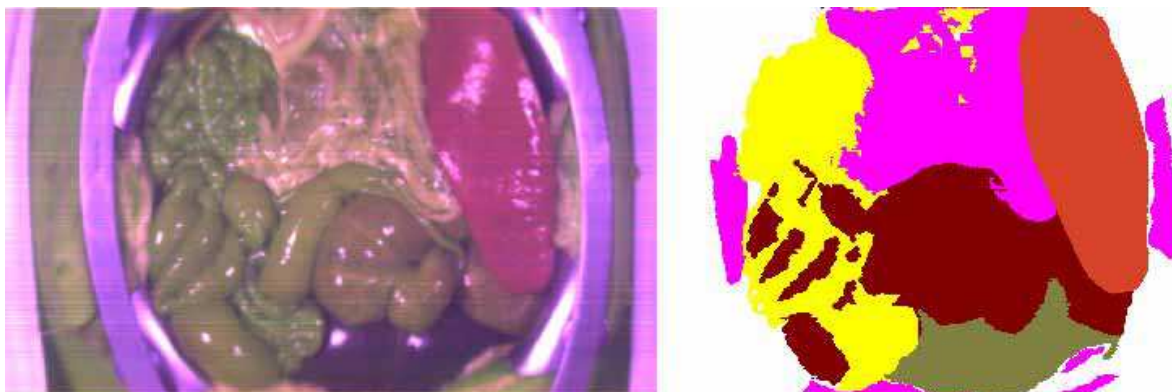

Fig. 12. The RGB image is made using three channels of near-infrared and infrared hyperspectral camera (900-1700 nm) is shown on the left side. Using LVQ method, the segmented image can be viewed on the right side. Spleen is shown in red, peritoneum in pink, urinary bladder in olive, colon in brown, and small intestine in yellow (Akbari et al., 2008a).

The hand-created maps were used as reference maps in calculating the detection rates of the method. Performance criteria for organ or tissue detection were the false negative rate (FNR) and the false positive rate (FPR), which were calculated for each organ. When a pixel was

not detected as an organ or tissue pixel, the detection was considered a false negative if the pixel was a pixel of that organ on the hand-created map. The FNR for an organ was defined as the number of false negative pixels divided by the total number of the organ pixels on the hand-created map. When a pixel was detected as an organ pixel, the detection was a false positive if the pixel was not an organ pixel on the hand-created map. The FPR was defined as the number of false positive pixels divided by the total number of non-organ pixels on the hand-created map. The pixels that were ambiguous and that the medical doctor could not label as an organ were not considered in our calculation. Figure 12 shows a segmented image using the LVQ method. The numerical results of the FPR and FNR for each organ and a comparison between LVQ and SVM methods (Akbari et al., 2008a; Akbari et al., 2009) are given in Table 1.

Camera & method	Organs	Spleen	Urinary Bladder	Peritoneum	Colon	Small Intestine
V10E (SVM)	FPR	3.9%	3.7%	5.3%	5.1%	8.7%
	FNR	4.5%	5.6%	7.3%	6.4%	7.2%
N17E (SVM)	FPR	1.1%	1.2%	4.3%	1.2%	7.3%
	FNR	1.3%	0.7%	5.1%	9.5%	2.7%
N17E (LVQ)	FPR	0.5%	1.3%	6.3%	1.2%	12.3%
	FNR	1.3%	1.4%	7.1%	15%	2.7%

Table 1. The evaluation results and comparison (Akbari et al., 2008a; Akbari et al., 2009)

The peritoneum has the highest value in visible and invisible wavelengths. The higher fat content of this tissue could be a possible explanation. In most spectral regions, the colon has the second highest reflectance value, after the peritoneum. In the colon, the adventitia forms small pouches filled with fatty tissue along the colon. The special histology and the fact that the urinary bladder is hollow inside, can explain the lowest spectral reflectance measured for this organ (Junqueira and Carneiro, 2005).

4. Intestinal Ischemia

Intestinal ischemia results from a variety of disorders that cause insufficient blood flow to the intestinal tract. The intestine like other live organs requires oxygen and other vital substances. These essential substances are delivered by arteries and carbon dioxide and other disposable substances are removed by veins. Intestinal ischemia results from decreasing the blood flow of the intestine to a critical point that delivery of oxygen is compromised. This problem results in intestinal dysfunction and ultimately necrosis. The prognosis of ischemic injuries depends on the quickness that the problem is brought to medical attention for diagnosis and treatment (Rosenthal & Brandt, 2007). Ischemia can be regional and limited to a small part of the intestine, or it may be more extensive. The intestinal ischemia may result from a shortage in blood passage through an artery or vein. There are several ways in which arterial or venous flows can be restricted: an embolus, a thrombus, or a poor blood flow through an artery or vein because of spasm in the blood vessel or clinical interventions (Rosenthal & Brandt, 2007).
Hyperspectral imaging may provide reliable data in near real-time with a convenient device for the surgeon in the operating room to diagnose the intestinal ischemia. In this section,

using the hyperspectral camera (900-1700nm), the spectral signatures for intestine, ischemic intestine and abdominal organs have been created. Using these signatures, the abdominal view through a large incision is segmented. Wavelet transform is used as the compression method and the SVM is used for classification.

4.1 Material and methods

ImSpector N17E is used to capture the hyperspectral data. The data are normalized to address the problem of spectral non-uniformity of the illumination device and influence of the dark current. The image digital numbers are normalized to yield the radiance of the specimen. The white reference and dark current were measured and raw data was normalized to these values as described in section 2.3.
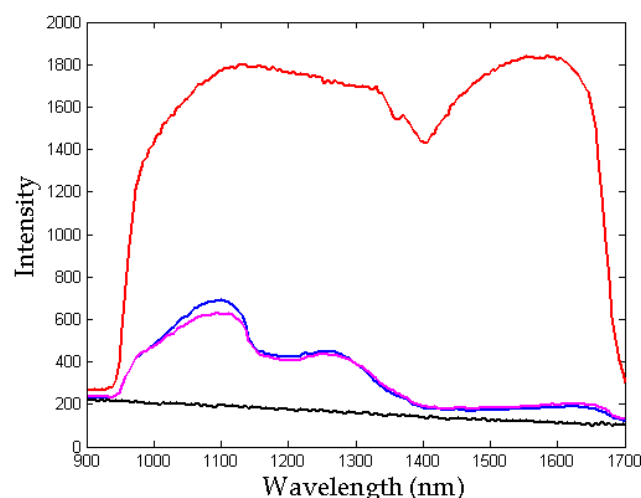

Fig. 13. The spectral signature of normal intestine, ischemic intestine, white reference, and dark current are shown in magnet, blue, red, and black, respectively.

The hyperspectral data are compressed using wavelet transform. Then the normal and ischemic loops of the intestine are segmented using SVM. The comparison of the spectral signatures of normal and ischemic regions of the intestine demonstrates a maximum difference in 1029-1136nm (see Figure 13). Since the main difference between normal and ischemic intestine is in the mentioned wavelength region, for discriminating the normal and ischemic tissues, these twenty two bands are used without compression. Some pixels which were lost because of glare are detected in post-processing. Since most of missed pixels were located at the mid portion of organs an image fill function is utilized as a post processing step. The hyperspectral images are compressed using wavelet transform. Each spectral signal is decomposed choosing the db3 (Daubechies-3) wavelet with level 2 compression (i.e. 1/4 compression). The compressed data are classified using SVM. Since the training data are not linearly separable, the kernel method is used in the study. The wavelet-based compressed pixel signatures are the input of SVM, and each input vector is to be assigned to one of two classes (intestine and non-intestine). In the next step, twenty two elements (1029-1136nm bands) of the original spectral data are the input vectors, and each input vector is to be assigned to one of ischemic or normal classes.

4.2 Experimental results

To perform the experiment, a pig was anesthetized. A large incision was created on the abdomen and intestine and other abdominal organs were explored. Vital signs were controlled during the surgery to guarantee a fairly constant oxygen delivery to the organs. An intestinal segment and the vessels supplying this segment were clamped for 6 minutes and the image was captured. The ImSpector N17E is fixed on the computer controlled linear actuator that was installed on a bridge over the surgical bed. The performance of the method was evaluated for detection of intestine and ischemic intestine. The evaluation was performed for the quality of detection in respect to hand-created maps. The hand-created maps are used as the reference maps in calculating the detection rates of the method. Performance criteria for intestine and ischemic intestine detection are false negative rate (FNR) and false positive rate (FPR). Figure 14 shows the ischemic intestinal pixels that are detected using the proposed method.
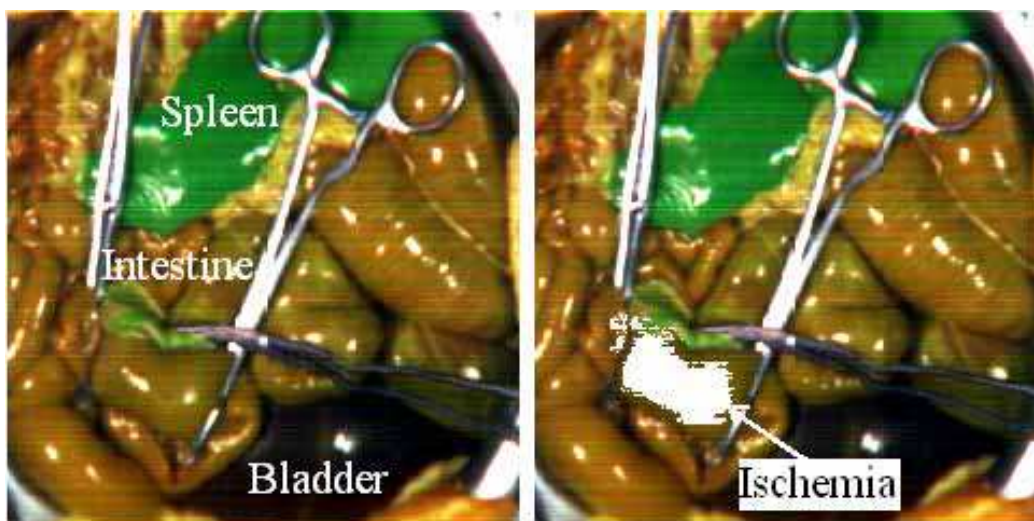

Fig. 14. An RGB image is made using three channels of the hyperspectral image. The detected ischemic intestinal tissue via the proposed method is shown with white (Akbari et al., 2008b).

In the first step, the algorithm detects intestinal pixels. When a pixel is not detected as an intestine pixel, the detection is a false negative if the pixel is a pixel of intestine on the hand-created map. FNR is defined as the number of false negative pixels divided by the total number of the non-intestine pixels on the hand-created map. When a pixel is not detected as an ischemic intestine pixel, the detection is a false negative if the pixel is a pixel of ischemic intestine on the hand-created map. FNR is defined as the number of false negative pixels divided by the total number of the normal intestine pixels on the hand-created map. In the second step, the ischemic intestinal pixels are detected. When a pixel is detected as an intestine pixel, the detection is a false positive if the pixel is not an intestine pixel on the hand-created map. FPR is defined as the number of false positive divided by the total number of intestine pixels on the hand-created map. When a pixel is detected as an ischemic intestine pixel, the detection is a false positive if the pixel is not an ischemic intestine pixel on the hand-created map. FPR is defined as the number of false positive divided by the total number of ischemic intestine pixels on the hand-created map. The ambiguous pixels that the

medical doctor can not label are eliminated in the calculation. The numerical results are given in Table 2 (Akbari et al., 2008b).

	Intestine	Ischemic Intestine
FPR	4.3%	2.3%
FNR	2.7%	9.7%

Table 2. The evaluation results of intestinal tissue and ischemic intestinal tissue detection (Akbari et al., 2008b).

5. Conclusions

This chapter described a new imaging method of hyperspectral imaging as a visual supporting tool during surgeries. Spectral signatures of various organs are presented and difference between normal and ischemic intestinal tissues is extracted. Large quantities of data in hyperspectral images can be processed to extend the range of wavelengths from visible to near infra and infra red wavelengths. This extension of the surgeon's vision would be a significant breakthrough. Capturing and visualizing the optical data of human organs and tissues can provide useful information for physicians and surgeons. This previously unseen information can be analyzed and displayed in an appropriate visual format. Hyperspectral imaging allows surgeons to less invasively examine a vast area without actually touching or removing tissue. A merit of this technique is the ability to both spatially and spectrally determine the differences among variant tissues or organs in surgery. The image-processing algorithms can incorporate detailed classification procedures that would be used for region extraction and identification of organs or tissues. Utilizing this technology in surgery will allow a novel exploration of anatomy and pathology, and may offer hope as a new tool for detection of tissue abnormalities.

6. References

Aikio, M. (2001). *Hyperspectral prism-grating-prism imaging spectrograph*, Espoo, Technical Research Centre of Finland, VTT publications, ISBN 951–38–5850–2, Finland

Akbari, H.; Kosugi, Y.; Kojima, K. & Tanaka, N. (2009). Hyperspectral image segmentation and its application in abdominal surgery, *International Journal of Functional Informatics and Personalized Medicine*, (Vol. 2, No. 2, pp. 201-216, ISSN (Online) 1756-2112 - ISSN (Print) 1756-2104)

Akbari, H.; Kosugi, Y.; Kojima, K. & Tanaka, N. (2008a). Wavelet-based Compression and Segmentation of Hyperspectral Images in Surgery, *Springer Lecture Notes in Computer Science (LNCS)*, Vol. 5125, pp. 142-149, ISSN 0302-9743

Akbari, H.; Kosugi, Y.; Kojima, K. & Tanaka, N. (2008b). Hyperspectral Imaging and Diagnosis of Intestinal Ischemia, *Proceedings of the 30th Annual International Conference of the IEEE Engineering in Medicine and Biology Society*, pp. 1238-1241, ISBN 978-1-4244-1814-5, Canada, August 2008, Vancouver

Bao, Y. & Liu Z. (2006). A fast grid search method in support vector regression forecasting time series, *LNCS 4224*, pp. 504-511, ISSN 0302-9743

Brown, M.; Lewis, H.G. & Gunn, S.R. (2000). Linear Spectral Mixture Models and Support Vector Machines for Remote Sensing, *IEEE Trans. Geosci. Remote Sens.* Vol. 38, No. 5, pp. 2346-2360, ISSN 0196-2892

Camps-Valls, G. & Bruzzone, L. (2005). Kernel-based methods for hyperspectral image classification, *IEEE Trans. Geosci. Remote Sens.,* Vol. 43, pp. 1351–1362, ISSN 0196-2892

Camps-Valls, G.; Gomez-Chova, L.; Calpe-Maravilla, J.; Martin-Guerrero, J. D.; Soria-Olivas, E.; Alonso-Chorda, L. & Moreno, J. (2004). Robust support vector method for hyperspectral data classification and knowledge discovery, *IEEE Trans. Geosci. Remote Sens.*, Vol. 42, No. 7, pp. 1530–1542, ISSN: 0196-2892

Cancio, L.C.; Batchinsky, A.I.; Mansfield, J.R.; Panasyuk, S.; Hetz, K.; Martini, D.; Jordan, B.S.; Tracey, B. & Freeman, J.E. (2006). Hyperspectral Imaging: A New Approach to the Diagnosis of Hemorrhagic Shock, *J. Trauma-Injury Infect. Crit. Care*, Vol. 60, No. 5, pp. 1087-1095, ISSN 1079-6061

Chui, C.K. (1993). *Wavelets: a tutorial in theory and applications,* Academic Press Professional, Inc., ISBN 0-12-174590-2, San Diego

Datt, B.; McVicar, T.R.; van Niel, T.G.; Jupp, D.L.B. & Pearlman, J.S. (2003). Preprocessing EO-1 hyperion hyperspectral data to support the application of agricultural indexes, *IEEE Trans. Geosci. Remote Sens.* Vol. 41, pp. 1246-1259, ISSN 0196-2892

Daubechies, I. (1992). *Ten lectures on wavelets*. Society for Industrial and Applied Mathematics, ISBN 0-89871-274-2, Philadelphia

Freeman, J.E.; Panasyuk, S.; Rogers, A.E.; Yang, S. & Lew, R. (2005). Advantages of intraoperative medical hyperspectral imaging (MHSI) for the evaluation of the breast cancer resection bed for residual tumor, *J. Clin. Oncol.*, Vol. 23, No. 16S, Part I of II (June 1 Supplement), p. 709, ISSN 1527-7755

Friedland, S.; Benaron, D.; Coogan, S.; Sze, D.Y. & Soetikno, R. (2007). Diagnosis of chronic mesenteric ischemia by visible light spectroscopy during endoscopy, *Gastrointestinal Endoscopy*, Vol. 65, No. 2, pp. 294-300, ISSN 0016-5107

Huang, C.; Davis, L. S.& Townshend, J. R. (2002). An assessment of support vector machines for land cover classification, *Int. J. Remote Sens.*, Vol. 23, No. 4, pp. 725–749, ISSN 0143-1161

Hughes, G. E. (1968). On the mean accuracy of statistical pattern Recognizers, *IEEE Trans. Inf. Theory*, Vol. 14, pp. 55–63, ISSN 0018-9448

Junqueira, L.C. & Carneiro, J. (2005). *Basic Histology: Text & Atlas*, McGraw-Hill Companies, ISBN-10 0071378294, USA

Kellicut, D.C.; Weiswasser, J.M.; Arora, S.; Freeman, J.E.; Lew, R.A.; Shuman, C.; Mansfield, J.R.& Sidawy, A.N. (2004). Emerging Technology: Hyperspectral Imaging, *Perspectives in Vascular Surgery and Endovascular Therapy*, Vol. 16, No. 1, pp. 53-57, ISSN 1531-0035

Khaodhiar, L.; Dinh, T.; Schomacker, K.T.; Panasyuk, S.V.; Freeman, J.E.; Lew, R.; Vo, T.; Panasyuk, A.A.; Lima, C.; Giurini, J.M.; Lyons, T.E.& Veves, A (2007). The Use of Medical Hyperspectral Technology to Evaluate Microcirculatory Changes in Diabetic Foot Ulcers and to Predict Clinical Outcomes, *Diabetes Care*, Vol. 30, No. 4, pp. 903-910, ISSN 1935-5548

Kohonen, T. (1987). *Self-Organization and Associative Memory*, Springer-verlag, ISBN 0-387-18314-0 2nd ed., Newyork

Lindsley, E.H.; Wachman, E.S. & Farkas, D.L. (2004). The hyperspectral imaging endoscope: a new tool for in vivo cancer detection, *Proceedings of the SPIE*, Vol. 5322, pp. 75-82, ISSN 0277-786X, USA, January 2004, San Jose

Liu, Z.; Yan, J.; Zhang, D. & Li, Q. (2007). Automated tongue segmentation in hyperspectral images for medicine, *Appl. Optics,* Vol. 46, No. 34, pp. 8328-8334, ISSN 0003-6935

Martin, M.E.; Wabuyele, M.B.; Chen, K.; Kasili, P.; Panjehpour, M.; Phan, M.; Overholt, B.; Cunningham, G.; Wilson, D.; Denovo, R.C.& Vo-dinh, T. (2006). Development of an advanced hyperspectral imaging (HSI) system with applications for cancer detection, *Annals of Biomedical Engineering*, Vol. 34, No. 6, pp. 1061–1068, ISSN 1521-6047

Melgani, F. & Bruzzone, L. (2004). Classification of hyperspectral remote sensing images with support vector machines, *IEEE Trans. Geosci. Remote Sens.*, Vol. 42, No. 8, pp. 1778–1790, ISSN 0196-2892

Monteiro, S.T.; Uto, K.; Kosugi, Y.; Kobayashi, N. & Watanabe, E. (2006). Optimization of infrared spectral manipulation for surgical visual aid, *Journal of Japan Society of Computer Aided Surgery*, Vol. 8, No. 1, pp. 33-38, ISSN 1344-9486

Moran, J.A.; Mitchell, A.K.; Goodmanson, G & Stockburger, K.A. (2000). Differentiation among effects of nitrogen fertilization treatments on conifer seedlings by foliar reflectance: a comparison of methods, *Tree Physiol.*, Vol. 20, pp. 1113–1120, ISSN 1758-4469

Poss, J. A.; Russell, W. B. & Grieve, C.M. (2006). Estimating yields of salt- and water-stressed forages with remote sensing in the, visible and near infrared, *J. Environ. Qual.*, Vol. 35, pp. 1060-1071, ISSN 1537-2537

Richardson, A.D.; Duigan S. P. & G. P Berlyn (2002). An evaluation of noninvasive methods to estimate foliar chlorophyll content, *New Phytol.*, Vol. 153, pp. 185-194, ISSN 0028-646X

Rosenthal, L. S. & Brandt L. J. (2007). *Intestinal Ischemia,* Albert Einstein College of Medicine, Montefiore Medical Center, The American College of Gastroenterology, Available: http://www.gi.org/patients/gihealth/pdf/ischemia.pdf

Suykens, J. A. K. & Vandewalle, J. (1999). Least squares support vector machine classifiers, *Neural Processing Letters,* Vol. 9, pp. 293-300, ISSN 1370-4621

Van Gestel, T.; Suykens, J.A.K.; Baesens, B.; Viaene, S.; Vanthienen, J.; Dedene, G.; De Moor, B. & Vandewalle, J. (2004). Benchmarking Least Squares Support Vector Machine Classifiers, *Machine Learning*, Vol. 54, No. 1, pp. 5-32, ISSN 0885-6125

Vapnik, V.N. (1995). *The nature of statistical learning theory,* Springer-Verlag, ISBN-10 0387987800, Berlin

Zuzak, K.J.; Naik, S.C.; Alexandrakis, G.; Hawkins, D.; Behbehani, K. & Livingston, E.H. (2007). Characterization of a near-infrared laparoscopic hyperspectral imaging system for minimally invasive surgery, *Anal. Chem.*, Vol. 79, pp. 4709-4715, ISSN 0003-2700

Recent Advances in Biomedical Engineering

Edited by Ganesh R Naik

The field of biomedical engineering has expanded markedly in the past ten years. This growth is supported by advances in biological science, which have created new opportunities for development of tools for diagnosis and therapy for human disease. The discipline focuses both on development of new biomaterials, analytical methodologies and on the application of concepts drawn from engineering, computing, mathematics, chemical and physical sciences to advance biomedical knowledge while improving the effectiveness and delivery of clinical medicine. Biomedical engineering now encompasses a range of fields of specialization including bioinstrumentation, bioimaging, biomechanics, biomaterials, and biomolecular engineering. Biomedical engineering covers recent advances in the growing field of biomedical technology, instrumentation, and administration. Contributions focus on theoretical and practical problems associated with the development of medical technology; the introduction of new engineering methods into public health; hospitals and patient care; the improvement of diagnosis and therapy; and biomedical information storage and retrieval. The book is directed at engineering students in their final year of undergraduate studies or in their graduate studies. Most undergraduate students majoring in biomedical engineering are faced with a decision, early in their program of study, regarding the field in which they would like to specialize. Each chosen specialty has a specific set of course requirements and is supplemented by wise selection of elective and supporting coursework. Also, many young students of biomedical engineering use independent research projects as a source of inspiration and preparation but have difficulty identifying research areas that are right for them. Therefore, a second goal of this book is to link knowledge of basic science and engineering to fields of specialization and current research. The editor would like to thank the authors, who have committed so much effort to the publication of this work.

How to reference

In order to correctly reference this scholarly work, feel free to copy and paste the following:

INTECH
open science | open minds

51000 Rijeka, Croatia
Phone: +385 (51) 770 447
Fax: +385 (51) 686 166
www.intechopen.com

中国上海市延安西路65号上海国际贵都大饭店办公楼405单元
Phone: +86-21-62489820
Fax: +86-21-62489821